Energy-dependent polarization study of the x-ray magnetic scattering in terbium metal

1998 J. Phys.: Condens. Matter 10 1951

(http://iopscience.iop.org/0953-8984/10/9/003)

J. Phys.: Condens. Matter **10** (1998) 1951–1964. Printed in the UK PII: S0953-8984(98)86914-2

Energy-dependent polarization study of the x-ray magnetic scattering in terbium metal

S C Perry†¶, M M R Costa‡, W G Stirling§, M J Longfield§, D Mannix§ and T Brückel‖

† Physics Department, School of Physical Science and Engineering, Keele University, Staffordshire ST5 5BG, UK
‡ Physics Department, Universidade de Coimbra, 3000 Coimbra, Portugal
§ Department of Physics, Oliver Lodge Laboratory, University of Liverpool, Liverpool L69 7ZE, UK
‖ HASYLAB, DESY, Notketstrasse 85, 22063 Hamburg, Germany

Received 13 August 1997

Abstract. A detailed study of the x-ray magnetic scattering from Tb has been performed, including polarization analysis of the scattered intensity as a function of energy close to the L_{II} and L_{III} absorption edges. Large enhancements of the magnetic signal are observed at these energies. It is found that the enhancement at the L_{III} edge is consistent with a simple dipole transition model, whereas the enhancement at the L_{II} edge shows an anomalous ∼5 eV splitting. The angular and polarization dependences of this resonance are investigated, and various explanations are discussed.

1. Introduction

1.1. X-ray resonant exchange scattering

It was pointed out by Blume in 1985 [1] that absorptive and dispersive contributions to the x-ray scattering cross section (so-called 'anomalous' terms) would cause interesting effects to occur when the incident energy is tuned close to an absorption edge of a magnetic element in the sample. X-ray resonant exchange scattering (XRES) at the holmium L_{III} edge was observed by Gibbs and co-workers in 1988 [2], and subsequently explained by Hannon *et al* [3] in terms of core-level electric dipole and quadrupole resonant transitions, to the 5d and 4f levels respectively. In simple terms, this resonant enhancement may be envisaged as the excitation by the incident photon of an inner-shell electron to an unoccupied level above the Fermi energy, which subsequently decays with the emission of an elastically scattered photon. The amplitude for the resonance then depends upon the overlap of the ground- and excited-state wave-functions coupled within optical selection rules. Besides the obvious advantage of a larger magnetic signal to aid the solution of complicated magnetic structures, such as was used in a recent study of Nd by Watson *et al* [4], the resonant cross section may be utilized to give detailed information on the fine structure of the magnetic states through detailed studies of the energy dependence of the magnetic scattering.

The contribution to the coherent scattering amplitude for an electric 2^L-pole resonance (EL) in a magnetic ion, with radiation of wave-vector $\boldsymbol{k}$ and polarization vector $\boldsymbol{\epsilon}$, is

¶ Present address: Department of Computer Science, University of Warwick, Coventry CV4 7AL, UK.

0953-8984/98/091951+14$19.50

given as [3]

$$f_{\mathrm{E}L}^{(\mathrm{XRES})}(\boldsymbol{k}'\boldsymbol{\epsilon}';\boldsymbol{k}\boldsymbol{\epsilon}) = \frac{4\pi}{|\boldsymbol{k}|} f_D \sum_{M=-L}^{L} \left[\hat{\boldsymbol{\epsilon}}'^{\star} \cdot \boldsymbol{Y}_{LM}^{(\epsilon)}(\hat{\boldsymbol{k}}') \boldsymbol{Y}_{LM}^{(\epsilon)\star}(\hat{\boldsymbol{k}}) \cdot \hat{\boldsymbol{\epsilon}}\right] F_{LM}^{(e)}(\omega) \qquad (1)$$

where f_D is the Debye–Waller factor and $\boldsymbol{Y}_{LM}^{(\epsilon)}(\hat{\boldsymbol{k}})$ are vector spherical harmonics, which determine the polarization dependence. The strength of the resonant enhancement is given by the factor $F_{LM}(\omega)$, which is dependent upon the atomic properties. Specifically, for an ion with initial state $|\alpha\rangle$ and excited state $|\eta\rangle$, this may be written as [3]

$$F_{LM}^{(e)}(\omega) = \sum_{\alpha,\eta}\left(\frac{P_\alpha P_\alpha(\eta)\Gamma_x(\alpha M\eta;\mathrm{E}L)/\,\Gamma(\eta)}{x(\alpha,\eta) - \mathrm{i}}\right) \qquad (2)$$

where P_α is the probability that the ion is in initial state $|\alpha\rangle$ and $P_\alpha(\eta)$ is the probability that the excited state $|\eta\rangle$ is initially unoccupied (determined by the overlap of the initial $|\alpha\rangle$ orbitals with those of the excited $|\eta\rangle$ state). The factor $\Gamma_x/\,\Gamma$ is the ratio of the linewidth for E*L radiative* decay from $|\eta\rangle \rightarrow |\alpha\rangle$ to the total width for all de-excitations of $|\eta\rangle$, which is equivalent to the fraction of photons which are elastically scattered. The denominator $x = (E_\eta - E_\alpha - \hbar\omega)/(\Gamma/2)$ measures the deviation from resonance in units of the *total* half-width.

1.2. XRES studies of terbium metal

The crystal structure of terbium metal is hexagonal close packed (HCP) containing two atoms per unit cell. The magnetic 4f shell contains eight electrons in a $^7\mathrm{F}_6$ ground state. The 5d and 6(s–p) conduction bands have energy widths between 5 and 10 eV; the 4f bands have energy widths of about 2 eV [5]. The spin structure undergoes a second-order phase transition from a paramagnetic (PM) phase to a basal-plane spiral antiferromagnetic (AF) phase at $T_N \sim 230$ K. At $T_C \sim 220$ K there is a second transition to a ferromagnetic (FM) phase [6]. In the AF region, magnetic satellites are situated at the $(0, 0, 2n \pm \tau)$ $(n = 0, 1, 2, \ldots)$ positions, with the modulation wave-vector (τ) proportional to the turn angle between planes.

The previous x-ray measurements [7, 8] of this material concentrated on the XRES at the $\mathrm{L_{III}}$ absorption edge. Both studies showed resonant behaviour of the magnetic signal near this edge and demonstrated how the integrated magnetic intensity increases and then decreases with decreasing temperature in the antiferromagnetic phase. In addition, weak spin-slip scattering was observed in the work of Gehring *et al* [8]. Neither study considered the $\mathrm{L_{II}}$-edge enhancements, an important feature of the current investigation.

2. Experimental details

The XRES measurements on Tb were performed at beam line W1 of the Hamburger Synchrotronstrahlungslabor (HASYLAB) in Germany. The sample used was a semi-cylindrical crystal, ∼8 mm long × 4 mm in diameter, with the *c*-direction perpendicular to the large cut face. It was grown at the University of Birmingham by D Fort. The sample mosaicity measured at the (0, 0, 4) charge peak using a Si analyser was 0.057° (FWHM). The sample was etched with a small amount of concentrated nitric acid (removed with acetone) before being mounted in a closed-cycle refrigerator. The temperature was stable to within ∼0.1 K at 225 K. A Si(Li) solid-state detector, without analyser, was used for measurements of the total scattered intensity; all of the reflections studied were

of the specular [0, 0, l] type, and the combination of incoming and outgoing slits gave a resolution width (FWHM) in the (0, 0, l) direction of 0.0068 reciprocal-lattice units (r.l.u.; 1 r.l.u. $(c^\star) = 1.1025$ Å^{-1}) measured at the (0, 0, 2) charge peak. The energy window of the detector apparatus was tuned around the elastic line at the Tb L_{III} (7514 eV) and L_{II} (8252 eV) edges using a multi-channel analyser. The energy resolution of the beam line was measured by rocking the second crystal of the double-bounce Si monochromator; it was found that $\Delta E/E = \cot\theta\,\Delta\theta = 2.2 \times 10^{-4}$.

Polarization analysis of the scattered intensity was achieved using a scintillation detector and a pyrolytic graphite (PG) crystal free to rotate about the axis of the scattered beam, as described previously [9]. The scattering angle from the PG (0, 0, 6) reflection is very close to 90° at both the L_{III} and L_{II} energies for Tb, as required for polarization analysis. The degree of linear polarization of the incoming beam ($P = [I_\sigma - I_\pi]/[I_\sigma + I_\pi]$) was measured by two scintillation counters mounted on the incoming beam tube to detect the air scattering in the σ- and π-channels; the average value of P throughout the beam lifetime was found to be $+91.2 \pm 0.2\%$. The Bragg angle of the PG was automatically adjusted at each energy, although its mosaic width was sufficiently large (0.25°) that it was not necessary to rock θ_{PG} at each point in the scan to obtain the full intensity.

The absorption of a 25 μm Tb metal foil was measured in transmission with two ion chambers around the L_{II} and L_{III} edges, in order to make absorption corrections. The first point of inflection of the edge was used to calibrate the energy scale of the monochromator. The energy calibration of the beam line was continuously monitored, using the solid-state detector and a second single-channel analyser to measure the fluorescence from the sample.

3. Results

3.1. The temperature dependence of the magnetic signal

An example scan of the $(0, 0, 2 + \tau)$ peak in the (0, 0, l) direction is shown in figure 1. This reflection was investigated as a function of temperature with XRES at the Tb L_{III} edge, and the results are shown in figure 2. The variation of τ over the AF phase, determined

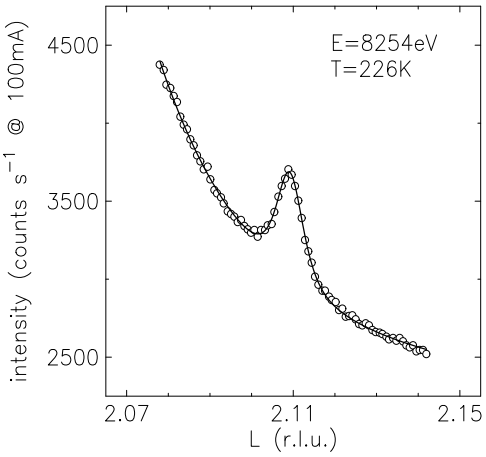

Figure 1. An $(0, 0, L)$ scan of the magnetic satellite at the L_{II} edge. Each datum point was counted for 20 seconds. The solid line is a fit of two Gaussian functions describing the magnetic peak and the background resulting from the (0, 0, 2) charge peak.

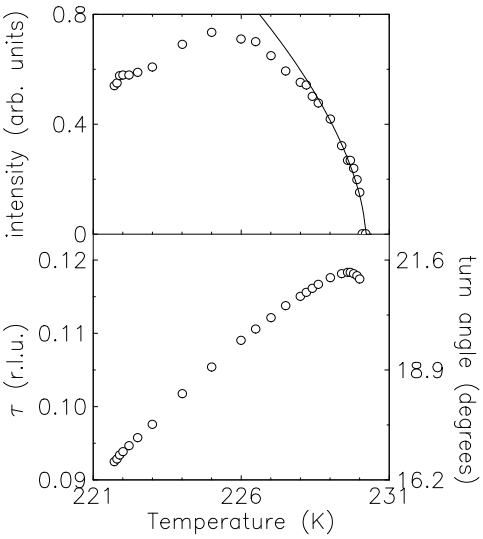

Figure 2. Bottom panel: the temperature dependence of the magnetic modulation wave-vector at the $(0, 0, 2 + \tau)$ satellite, as determined from fits of the type shown in figure 1. The values shown have not been corrected for the lattice expansion, but Gehring *et al* [8] have shown that the error in the measurement from this effect is $\leqslant 0.0002$ r.l.u. The overall errors in the measurements are smaller than the points. 1 r.l.u. for the $c^\star$-direction $= 1.1025$ Å^{-1}. Top panel: the variation of integrated intensity of the $(0, 0, 2 + \tau)$ satellite as a function of temperature. The solid line is a fit described in the text.

by measuring the wave-vector of the $(0, 0, 2 + \tau)$ reflection, is shown in the lower panel of figure 2; it is found to lie between 0.0925 and 0.1183 r.l.u. This corresponds to a turn angle per layer of 16.7° to 21.3°. The downturn of the modulation wave-vector as the PM phase is approached is clearly visible, as in previous x-ray and neutron studies [7, 8, 10, 11]. The variation of the magnetic intensity is shown in the top panel of figure 2. The increase in the magnetic intensity at the onset of the AF phase is clearly shown, as is the reduction in intensity as the FM phase is approached.

The dominant contribution to the resonant dipole (E1) scattering length has been shown [12] to be proportional to the magnetic moment (as in neutron diffraction); this allows one to measure the sublattice magnetization critical exponent ($\beta = \lim_{t\to 0}(\log I/\log t)$) from magnetic Bragg intensities. The dipolar nature of this resonance is discussed in section 3.2. The measurements should ideally be made as close to the transition temperature, T_N, as possible; this is especially important in the present case due to the influence of the second phase transition to the FM phase. The value from the fit shown in figure 2 was $\beta = 0.3 \pm 0.07$, with $T_N = 230.2 \pm 0.1$. This was obtained using ten datum points with $T > 228.5$ K; when larger temperature ranges were used the value of β was reduced, to ~ 0.2 for fits in the range $T > 225$ K. Detailed measurements of the magnetic signal very close to the transition temperature will be required before this exponent can be measured with greater precision.

3.2. The energy dependence of the resonant intensity

The sample was cooled to a temperature of 226 K, and the integrated intensity of the magnetic signal was measured as a function of energy close to the L_{II} and L_{III} absorption

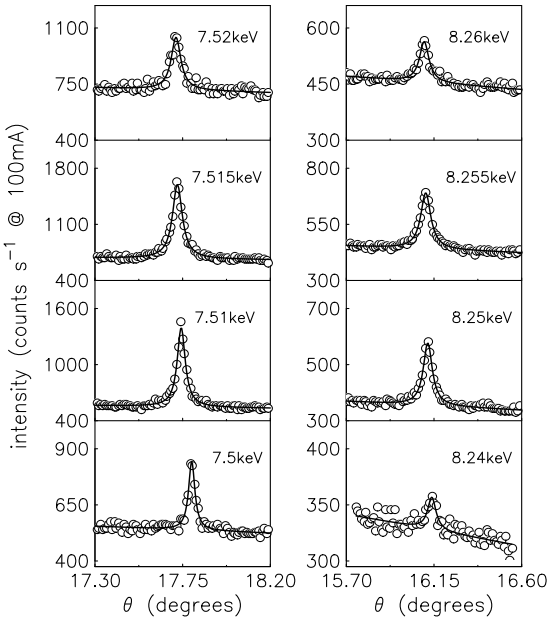

Figure 3. θ rocks through the $(0, 0, 2+\tau)$ magnetic satellite with the incident energy tuned close to the L_{III} (left-hand side) and L_{II} (right-hand side) absorption edges. The peaks are well described by simple Lorentzian functions on sloping backgrounds, as shown by the solid lines in the diagram.

edges by means of rocking curves through the peak, as shown in figure 3. As well as the total intensity of the peak, the scattering was also measured in the $\sigma \rightarrow \sigma$ and $\sigma \rightarrow \pi$ channels separately for some of the reflections.

The strongest enhancement of the magnetic signal occurs at the L_{III} edge, as demonstrated on the left-hand side of figure 3. The intensity of the total scattering from the $(0, 0, 2+\tau)$ and $(0, 0, 2+2\tau)$ reflections is shown in the bottom panel of figure 4. Corrections for sample absorption have been made assuming the infinite-flat-plate geometry, and the intensities are simply multiplied by the absorption coefficient. The profile of the XRES from the $(0, 0, 2+\tau)$ satellite close to the L_{III} edge becomes much more symmetric once the correction for sample absorption has been made, although there is still a slight asymmetry. This may be due to the non-resonant terms in the magnetic cross section, which are not considered in this paper. The solid lines in the figure show least-squares fits of the data to a function of the form

$$I(E) \propto |f_{E1}|^2 \propto 1 \Big/ \left| \frac{E_r - \hbar\omega}{\Gamma/2} - \mathrm{i} \right|^2 = 1 \Big/ \left(\left[\frac{E_r - \hbar\omega}{\Gamma/2} \right]^2 + 1 \right) \tag{3}$$

convoluted with a Gaussian function of width 1.6 eV (FWHM) to represent the energy resolution of the instrument at 7.514 keV. The width of the $(0, 0, 2+\tau)$ XRES profile is then found to be 6.9 ± 0.2 eV (FWHM) corresponding to a lifetime of the excited state of $\sim$0.1 fs. The very weak nature of the $(0, 0, 2+2\tau)$ reflection means that the statistical quality of the data is limited, but this profile seems to have the same width and position. In both cases, the centre of the resonance is observed at 2.13 ± 0.08 eV above the absorption edge. The ratio of the intensities of the first- and second-order satellites is $\sim$1000. Following

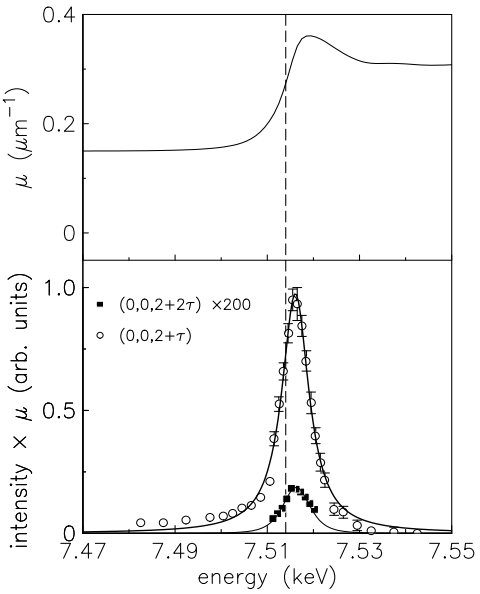

Figure 4. The energy dependence of the resonant enhancement close to the L_{III} edge (7514 eV). The top panel shows the measured absorption coefficient; the bottom panel shows integrated intensities of the total scattering, corrected for absorption, of the $(0, 0, 2+\tau)$ and $(0, 0, 2+2\tau)$ reflections. The $(0, 0, 2+2\tau)$ data have been scaled by a factor of 200, for clarity. The dashed line marks the position of the L_{III} edge; the solid lines are fits described in the text.

Hill and McMorrow [13] (HM), this can be used to give the ratio of the matrix elements:

$$\frac{F_{E1}^{(1)}}{F_{E1}^{(2)}} = \sqrt{\frac{\sim 1000}{4}\frac{1+\sin^2\theta}{\cos^2\theta}} \sim 17. \tag{4}$$

The results for holmium of Gibbs *et al* [14] (their figure 8) give this intensity ratio as approximately 30, which leads to a ratio of the matrix elements of $\sim$2.7 [13].

The intensity of the scattering in the two polarization channels is shown in figure 5. The energy steps are wider than in the total intensity data. The data are not corrected for absorption. The scattering appears to lie only in the $\sigma \rightarrow \pi$ channel throughout the resonance; the small amount of scattering in the other channel is attributed to the 5% π-polarized component of the incident beam (as is usual with measurements of this nature; see for example the holmium study [14]).

The above results suggest that the resonance close to the L_{III} edge in Tb arises from a simple dipolar transition from a 2p core level to the 5d conduction band. The XRES dipolar cross section contains no terms of order greater than 2; however, we have observed evidence of a peak at the $(0, 0, 2+3\tau)$ position (figure 6). The very weak nature of this feature prevented a full investigation from being performed, but it does appear to be strongly temperature dependent. One of the simplest explanations for this effect is that it is due to a slight 'squaring' of the sinusoidal modulation as the ferromagnetic phase is approached. It is also possible that this 3τ feature is of a quadrupolar (E2) nature since this would be expected to vary with the third power of the ordered moment and hence have a very strong dependence on temperature; the corresponding E2 contribution at the first-order satellite would be 'masked' by the much stronger E1 component [15].

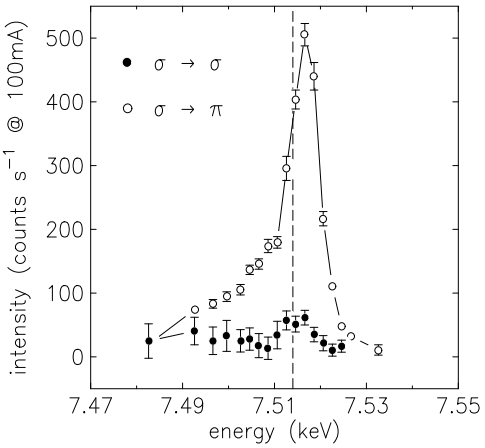

Figure 5. The energy dependence of the $(0,\ 0,\ 2+\tau)$ satellite close to the L_{III} edge, with the polarization channels separated. These data have not been corrected for absorption. The statistical quality of the $\sigma \rightarrow \sigma$ data is significantly worse due to the increased background from the charge peak and from inelastic scattering in this channel. The full line is a guide to the eye.

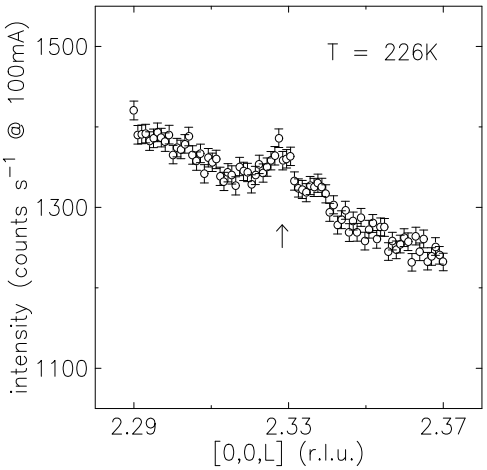

Figure 6. An $(0, 0, L)$ scan at the L_{III}-edge energy. The arrow marks the expected position of the $+3\tau$ satellite.

In contrast to the simple nature of the resonant profile close to the L_{III} edge, the magnetic intensity close to the L_{II} edge has complex energy and wave-vector dependencies. The intensities of the $(0, 0, 2+\tau)$, $(0, 0, 4-\tau)$ and $(0, 0, 4+\tau)$ satellites, which were obtained by integrating separate rocking curves through the peaks at each energy, are shown in figure 7. Again the data have been corrected for sample absorption, although the effect of this correction is less dramatic than at the L_{III} edge, as expected from comparison of the absorption profiles for the two energies (the top panels of figures 4 and 7). The most striking feature of the resonant profile near the L_{II} edge is its double-peaked nature, which has been confirmed in several independent experiments.

The polarization dependence of the scattering at the $(0, 0, 2+\tau)$ reflection was examined,

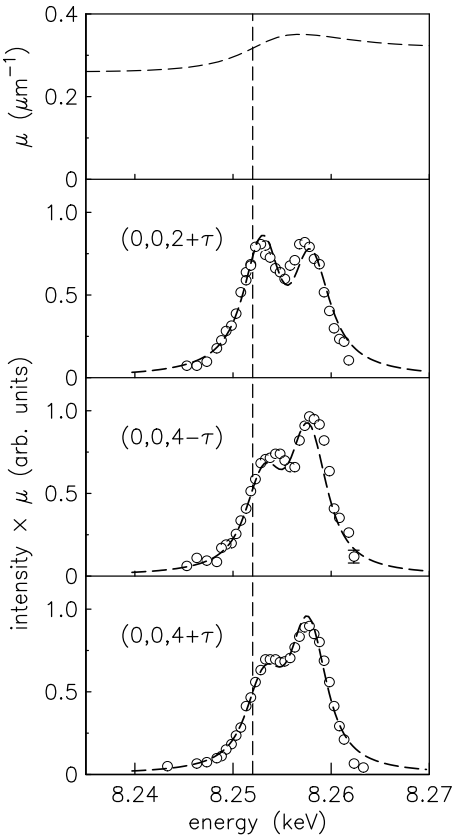

Figure 7. The energy dependence of the first-order satellite close to the L_{II} edge (8252 eV) for different wave-vectors. The dashed lines are from a fit described in the text (section 4).

and the intensity of the signal in the two polarization channels is shown in figure 8. It is clear that most of the scattering lies in the $\sigma \rightarrow \pi$ channel, although there is some structure in this channel, and a slight increase in the intensity in the $\sigma \rightarrow \sigma$ channel, at ∼8.257 keV.

4. Discussion

We now consider the origin of the effects discussed above. Whereas the L_{III}-edge scattering appears to be satisfactorily explained by a simple dipolar resonance, the interpretation of the XRES data for the L_{II} edge presents some interesting questions. The accepted view of the electronic structure in the rare earths is that the energies of the (quadrupolar) excitations to the 4f levels are lower than those of the (dipolar) excitations to the 5d levels, as demonstrated by the XRES measurements at the L_{III} edge in Ho [14]. However, there is a problem as regards reconciling this view with the accepted form of the XRES cross section and the experimental measurements, as detailed below.

The polarization dependence of a particular resonance is found by expanding the spherical harmonic term in equation (1). This has been performed for electric dipole (E1) and quadrupole (E2) transitions in HM in a way particularly suited to synchrotron experiments, by writing the operators as 2×2 matrices with polarization states chosen either parallel or

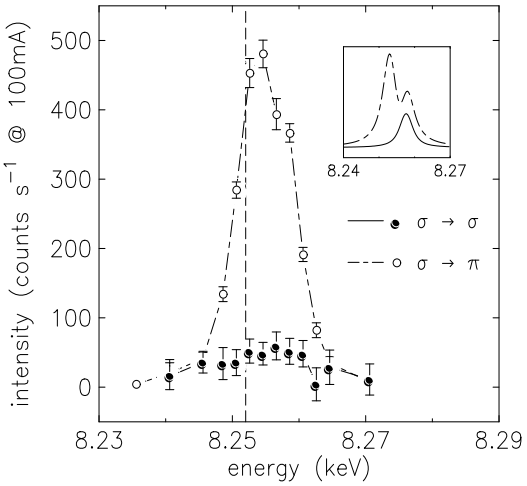

Figure 8. The energy dependence of the $(0, 0, 2 + \tau)$ satellite close to the L_{II} edge, with polarization channels separated. Again, these data have not been corrected for absorption. The inset shows the results for the intensity in the separate channels calculated using the values from the fit in figure 7. The chain line through the data is a guide to the eye.

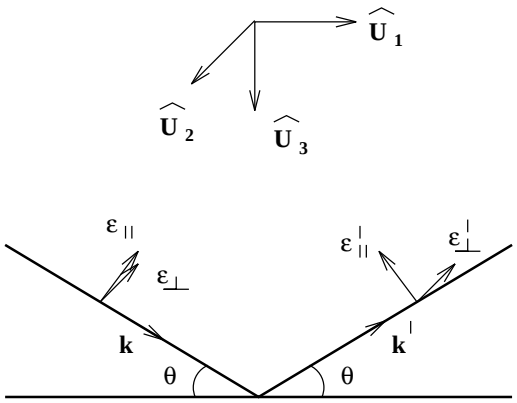

Figure 9. A diagram defining the wave-vectors $\boldsymbol{k}$ and $\boldsymbol{k}'$ and the polarization vectors $\boldsymbol{\epsilon}_\perp$, $\boldsymbol{\epsilon}_\parallel$, $\boldsymbol{\epsilon}'_\perp$ and $\boldsymbol{\epsilon}'_\parallel$ for the incident and diffracted beams. The diffraction plane is spanned by the $\hat{\boldsymbol{U}}_1$- and $\hat{\boldsymbol{U}}_3$-axes; the Bragg angle is θ.

perpendicular to the scattering plane (as shown in figure 9). The convention of referring to radiation linearly polarized in the plane of the synchrotron as σ-polarized, and radiation linearly polarized in the scattering plane (perpendicular to the plane of the synchrotron) as π-polarized, will be adopted here, as in HM. The electric dipole scattering amplitude is found to be [13]

$$f_{n\mathrm{E1}}^{\mathrm{XRES}} = F_{\mathrm{E1}}^{(0)} \begin{pmatrix} 1 & 0 \\ 0 & \cos 2\theta \end{pmatrix} - \mathrm{i}F_{\mathrm{E1}}^{(1)} \begin{pmatrix} 0 & z_1 \cos\theta + z_3 \sin\theta \\ z_3 \sin\theta - z_1 \cos\theta & -z_2 \sin 2\theta \end{pmatrix} + F_{\mathrm{E1}}^{(2)} \begin{pmatrix} z_2^2 & -z_2(z_1 \sin\theta - z_3 \cos\theta) \\ z_2(z_1 \sin\theta + z_3 \cos\theta) & -\cos^2\theta(z_1^2 \tan^2\theta + z_3^2) \end{pmatrix} \tag{5}$$

where z_U are the components of the unit magnetic moment of the ion, and $F_{\mathrm{E1}}^{(Y)}$ are linear

combinations of the F_{LM}-factors allowed by the E1 selection rules. The individual terms in the matrices then represent the contribution to the $\sigma \rightarrow \sigma$, $\sigma \rightarrow \pi$, $\pi \rightarrow \sigma$ and $\pi \rightarrow \pi$ components respectively. The term in $F^{(0)}$ has no dependence on the magnetic moment and contributes only to the charge scattering. A similar but much longer expression is available for the quadrupole term, for which the reader is referred to HM [13].

The magnetic moment of the basal-plane spiral AF, for the case of the modulation wave-vector pointing along the $\hat{\boldsymbol{U}}_3$-axis, may be written as

$$\hat{\boldsymbol{z}}_n = \cos(\boldsymbol{\tau} \cdot \boldsymbol{r}_n)\hat{\boldsymbol{U}}_1 + \sin(\boldsymbol{\tau} \cdot \boldsymbol{r}_n)\hat{\boldsymbol{U}}_2. \tag{6}$$

The fact that there is no $\hat{\boldsymbol{U}}_3$-component to the magnetic moment means that all terms in z_3 drop out of equation (5) and one may write the expression for the XRES scattering amplitude [13] as

$$f_{\mathrm{E1}}^{\mathrm{XRES}} = \begin{pmatrix} z_2^2 F_{\mathrm{E1}}^{(2)} & -\mathrm{i}z_1 \cos\theta F_{\mathrm{E1}}^{(1)} - z_2 z_1 \sin\theta F_{\mathrm{E1}}^{(2)} \\ \mathrm{i}z_1 \cos\theta F_{\mathrm{E1}}^{(1)} + z_2 z_1 \sin\theta F_{\mathrm{E1}}^{(2)} & \mathrm{i}z_2 \sin 2\theta F_{\mathrm{E1}}^{(1)} - z_1^2 \sin^2\theta F_{\mathrm{E1}}^{(2)} \end{pmatrix}. \tag{7}$$

For simplicity we consider the incident beam to be linearly polarized perpendicular to the scattering plane, so that only the $\sigma \rightarrow \sigma$ and $\sigma \rightarrow \pi$ channels contribute, as in previous treatments [14]. This leads to the following expressions for the dipole scattering amplitudes in the two polarization channels [13]:

$$f_{n\mathrm{E1}}^{\sigma\rightarrow\sigma} = F_{\mathrm{E1}}^{(2)}\left(\frac{1}{2} - \frac{\mathrm{e}^{\pm 2\mathrm{i}\boldsymbol{\tau}\cdot\boldsymbol{r}}}{4}\right) \tag{8}$$

$$f_{n\mathrm{E1}}^{\sigma\rightarrow\pi} = -F_{\mathrm{E1}}^{(1)}\,\mathrm{i}\cos\theta\frac{\mathrm{e}^{\pm\mathrm{i}\boldsymbol{\tau}\cdot\boldsymbol{r}}}{2} \mp F_{\mathrm{E1}}^{(2)}\sin\theta\frac{\mathrm{e}^{\pm 2\mathrm{i}\boldsymbol{\tau}\cdot\boldsymbol{r}}}{4}. \tag{9}$$

For the $\sigma \rightarrow \sigma$ scattering, the first term in equation (8) is zeroth order, resulting from the square of z_2, and contributes extra scattering at the charge Bragg peak. The second term is second order and contributes to the magnetic satellite at $\pm 2\tau$ either side of the charge peak along the $\hat{\boldsymbol{U}}_3$-direction. For the $\sigma \rightarrow \pi$ channel the first term in equation (9) is first order and produces scattering at $\pm\tau$; the second term then produces additional scattering at $\pm 2\tau$. The XRES dipole scattering at $\pm\tau$ is therefore purely $\sigma \rightarrow \pi$ polarized. The combination of equations (8) and (9) was used to obtain the ratio of the matrix elements in equation (4).

A similar treatment for the quadrupole transition is much longer and gives terms in zeroth, first, second, third and fourth order; for the sake of brevity we will consider only the first- and second-order terms. The quadrupole scattering amplitudes for a basal-plane spiral are

$$\begin{aligned} f_{n\mathrm{E2}}^{\sigma\rightarrow\sigma} = {} & \left[\pm F_{\mathrm{E2}}^{(1)}\frac{\sin 2\theta}{2} \pm 3\mathrm{i}(F_{\mathrm{E2}}^{(3)} - F_{\mathrm{E2}}^{(1)})\frac{\sin 2\theta}{8} \mp \mathrm{i}F_{\mathrm{E2}}^{(3)}\frac{\sin 2\theta}{8}\right]\mathrm{e}^{\pm\mathrm{i}\boldsymbol{\tau}\cdot\boldsymbol{r}} \\ & + \left[(F_{\mathrm{E2}}^{(2)} - F_{\mathrm{E2}}^{(0)})\left\{\frac{\cos^2\theta}{4} - \frac{\cos 2\theta}{4}\right\}\right]\mathrm{e}^{\pm 2\mathrm{i}\boldsymbol{\tau}\cdot\boldsymbol{r}} \end{aligned} \tag{10}$$

$$\begin{aligned} f_{n\mathrm{E2}}^{\sigma\rightarrow\pi} = {} & \left[-F_{\mathrm{E2}}^{(1)}\frac{\mathrm{i}\cos\theta\cos 2\theta}{2} - (F_{\mathrm{E2}}^{(3)} - F_{\mathrm{E2}}^{(1)})\left\{\frac{3\mathrm{i}\cos^3\theta}{8} + \frac{\mathrm{i}\sin\theta\sin 2\theta}{8}\right\}\right. \\ & \left. + F_{\mathrm{E2}}^{(3)}\left\{\frac{\mathrm{i}\cos\theta\cos 2\theta}{8} + \frac{3\mathrm{i}\cos\theta\sin^2\theta}{8}\right\}\right]\mathrm{e}^{\pm\mathrm{i}\boldsymbol{\tau}\cdot\boldsymbol{r}} \\ & + \left[\mp(F_{\mathrm{E2}}^{(2)} - F_{\mathrm{E2}}^{(0)})\frac{\sin\theta\cos 2\theta}{4} \mp F_{\mathrm{E2}}^{(2)}\frac{\cos\theta\sin 2\theta}{4}\right. \\ & \left. \pm F_{\mathrm{E2}}^{(0)}\frac{\cos\theta\sin 2\theta}{4} \mp F_{\mathrm{E2}}^{(4)}\frac{\sin\theta\cos^2\theta}{8}\right]\mathrm{e}^{\pm 2\mathrm{i}\boldsymbol{\tau}\cdot\boldsymbol{r}}. \end{aligned} \tag{11}$$

Comparison of equation (9) with equations (10) and (11) shows that the XRES amplitude for the first-order satellite is much more complicated in the quadrupole case, having components in both polarization channels and a complicated angular dependence.

Inspection of figure 7 suggests a different interpretation of the nature of the resonances at the Tb L_{II} edge from that for those at the Ho L_{III} edge. The lower-energy peak at the Tb L_{II} edge *decreases* in strength with *increasing* wave-vector (or, equivalently, with 2θ). This would suggest that the lower-energy peak has a dipolar origin (following equation (9)), whereas the higher-energy peak may be of quadrupolar nature.

The model for the energy dependence of the integrated intensity, including both dipole and quadrupole contributions, has the form

$$\begin{aligned} I(E) &\propto \left|f_{\mathrm{E2}}^{\sigma\to\sigma}\right|^2 + \left|f_{\mathrm{E1}}^{\sigma\to\pi} + f_{\mathrm{E2}}^{\sigma\to\pi}\right|^2 \\ &\propto \left|\mathcal{A}_{\sigma\to\sigma}\Big/\left(\frac{E_{\mathcal{A}}-\hbar\omega}{\Gamma/2}-\mathrm{i}\right)\right|^2 \\ &\quad + \left|\mathcal{A}_{\sigma\to\pi}\Big/\left(\frac{E_{\mathcal{A}}-\hbar\omega}{\Gamma/2}-\mathrm{i}\right) + \mathcal{B}_{\sigma\to\pi}\Big/\left(\frac{E_{\mathcal{B}}-\hbar\omega}{\Gamma/2}-\mathrm{i}\right)\right|^2 \end{aligned} \tag{12}$$

where $\mathcal{A}_{\sigma\to\sigma}$, $\mathcal{A}_{\sigma\to\pi}$ and $E_{\mathcal{A}}$ are the amplitudes and resonant energy respectively of the quadrupole transition, and $\mathcal{B}_{\sigma\to\pi}$ and $E_{\mathcal{B}}$ are the amplitude and resonant energy of the dipole transition. This function may be used to give the form of the resonance at a particular wave-vector. The amplitudes in equation (12) are given as a function of wave-vector by equations (9), (10) and (11), and may be combined to describe the scattering as a function of energy *and* wave-vector. A fit of this type (when convoluted with a Gaussian function of width 1.8 eV (FWHM) to represent the energy resolution at 8.252 keV) is shown by the dashed lines in figure 7; it is stressed that this fit was carried out *simultaneously* to the scattering at all three reflections as a function of energy *and* wave-vector. The only satisfactory description of the data gives the dipole energy at 1.23 ± 0.04 eV below the absorption edge and the quadrupole energy at 5.62 ± 0.04 eV above the edge. *No satisfactory fit could be obtained with the quadrupole energy lower than the dipole energy.* To minimize the number of floating parameters in the fit, the widths of the peaks were held constant; this resonance width was found to be 3.66 ± 0.04 eV, corresponding to a lifetime of $\sim$0.2 fs (although in theory it is possible for the dipolar and quadrupolar terms to have different lifetimes).

The ratios of the matrix elements from the above fit were found to be

$$\frac{F_{\mathrm{E2}}^{(1)}}{F_{\mathrm{E2}}^{(3)}} = 1.10 \pm 0.03 \tag{13}$$

$$\frac{F_{\mathrm{E1}}^{(1)}}{F_{\mathrm{E2}}^{(1)}} = 0.86 \pm 0.01. \tag{14}$$

These ratios have been used, with equations (9), (10) and (11), to calculate the angular dependences of the first-order satellite for dipole and quadrupole resonances in terbium, and are shown in figure 10. It should be noted that the shape of the quadrupolar angular dependence remains qualitatively the same for any ratio $F_{\mathrm{E2}}^{(1)}/F_{\mathrm{E2}}^{(3)}$. The dashed lines in the figure represent the positions of the three reflections measured. The increase in the strength of the quadrupole term with wave-vector at the three positions provides a justification for the identification of the higher excitation as quadrupolar.

The bottom panel of figure 10 shows the angular dependence for the separated polarization channels of the quadrupolar transition, calculated using the ratio for the quadrupole matrix elements from equation (13). It is clear from this figure that for the

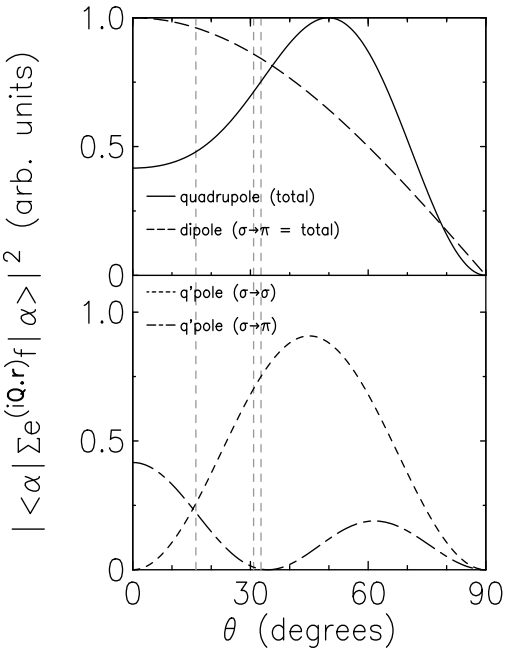

Figure 10. The angular dependence of the first-order satellite for a basal-plane spiral. The dipole and quadrupole terms have been normalized to the same peak intensity. The vertical dashed lines mark the positions of the $(0, 0, 2 + \tau)$, $(0, 0, 4 - \tau)$ and $(0, 0, 4 + \tau)$ reflections, respectively, at the L_{II} edge.

$(0, 0, 2 + \tau)$ satellite ($\theta \sim 16.2^\circ$), the intensity in the $\sigma \rightarrow \sigma$ channel is expected to be comparable with that in the $\sigma \rightarrow \pi$ channel, for a purely quadrupole transition. The inset to figure 8 shows the calculated overall intensities in the separate channels for the dipole and quadrupole contributions. Although there appears to be some structure in the $\sigma \rightarrow \pi$ data where the higher-energy peak appears, the $\sigma \rightarrow \sigma$ data are not consistent with the appreciable peak predicted by the model calculations whose results are shown in the inset. Unfortunately, polarization analysis was not performed for the other reflections. Although the scattering in the $\sigma \rightarrow \sigma$ channel is more difficult to measure due to the increased background from the charge peak, successful polarization experiments have been performed under similar circumstances at beam line W1 in the past, and we have no reason to doubt the validity of this measurement. So, on the basis of the angular dependence of the L_{II} signal, one might be led to the identification of the upper peak as of quadrupolar origin, but the polarization analysis data are not consistent with this interpretation.

However, very recent calculations by Lovesey *et al* [15] do support this identification. These authors calculated the quadrupolar contributions to the scattering length, with approximations consistent with the standard sum rules employed in the analysis of absorption data. These calculations are thus of direct relevance to the observations discussed in this paper. What they find is that the E2 scattering at the L_{III} edge of Tb decreases in intensity with increasing 2θ, while at the L_{II} edge the E2 intensity *increases* somewhat over the range of the measurements. The upper energy peak of figure 7 behaves in this latter manner. However, the calculations of reference [15] suggest that the E2 scattering at the L_{III} edge (where the dipolar E1 scattering will be dominant) should be much stronger than that at the L_{II} edge. Nevertheless, these new calculations do provide some justification for the above

E1/E2 identification at the L_{II} edge.

An alternative identification of the two peaks is that they are both dipolar in nature, presumably due to some splitting in the 5d levels. Support for this contention is provided by the spin-dependent photoabsorption measurements of Schütz *et al* [16]. For a polycrystalline foil of Tb in the ferromagnetic state, the L_{III} spin-dependent absorption spectrum exhibits a single feature just above the edge, whereas at the L_{II} edge a split feature (with a splitting of about 5 eV) was observed. Identification of the observed energy profiles as split-dipole resonances would account for the lack of $\sigma \rightarrow \sigma$ scattering at the $(0, 0, 2 + \tau)$ reflection. However, there are problems as regards reconciling this explanation with the different angular dependences of the two components. Detailed self-consistent-field calculations would be useful for gaining a fuller understanding of these observations.

5. Conclusion

Study of the magnetic properties of rare-earth antiferromagnets with x-ray resonant enhanced scattering is interesting in a number of ways. Clearly, the advantage of increased intensity coupled with the inherent benefits of x-ray scattering (high wave-vector resolution, total energy integration) offer a technique complementary to neutron scattering in the study of magnetic structures and their evolution. In this paper we have presented a very accurate measurement of the modulation of the magnetic spiral in terbium as a function of temperature.

Another aspect of XRES study is the ability to probe directly the electronic states above the Fermi surface in the magnetic ion. As demonstrated in this paper, the ratios of linear combinations of matrix elements, which measure the overlap of the ground- and resonant-state wave-functions, are obtainable from measurements of the magnetic intensity as a function of energy and wave-vector. These determinations could be further improved by measuring more magnetic satellites, and by making accurate measurements of the polarization at each reflection. Such measurements, which are planned for the near future, might lead to an understanding of the apparent anomalous splitting observed at the L_{II} edge of terbium at each reflection. Precise predictions for the polarization behaviour of the E2 scattering at the L_{III} and L_{II} edges are made in the work of reference [15].

Acknowledgments

The authors are particularly grateful to S W Lovesey for detailed discussions of the role of quadrupolar scattering in terbium. We also wish to thank W J Nuttall, P Strange, D Gibbs, S P Collins and G H Lander for helpful discussions. The experiments at HASYLAB were motivated and funded by the European Community Human Capital Mobility and SCIENCE programmes; we gratefully acknowledge this support. SCP, WGS, MJL and DM are grateful to the UK Engineering and Physical Sciences Research Council for financial assistance.

References

[1] Blume M 1985 *J. Appl. Phys.* **57** 3615
[2] Gibbs D, Harshman D R, Isaacs E D, McWhan D B, Mills D and Vettier C 1988 *Phys. Rev. Lett.* **61** 1241
[3] Hannon J P, Trammell G T, Blume M and Gibbs D 1988 *Phys. Rev. Lett.* **61** 1245
[4] Watson D, Forgan E M, Nuttall W J, Stirling W G and Fort D 1996 *Phys. Rev.* B **53** 726
[5] Lang J K, Bauer Y and Cox P A 1981 *J. Phys. F: Met. Phys.* **11** 121

[6] Sinha S K 1978 Magnetic structures and inelastic neutron scattering *Handbook on the Physics and Chemistry of Rare Earths* vol 1, ed G A Gschneidner and L Eyring (Amsterdam: North-Holland) ch 7
[7] Tang C C, Stirling W G, Jones D L, Wilson C C, Haycock P W, Rollason A J, Thomas A H and Fort D 1992 *J. Magn. Magn. Mater.* **103** 86
[8] Gehring P M, Rebelsky L, Gibbs D and Shirane G 1992 *Phys. Rev.* B **45** 243
[9] Brückel T, Lippert M, Köhler T, Schneider J R, Prandl W, Rilling V and Schilling M 1996 *Acta Crystallogr.* A 427
[10] Koehler W C 1965 *J. Appl. Phys.* **36** 1078
[11] Dietrich O W and Als-Nielsen J 1967 *Phys. Rev.* **162** 315
[12] Luo J, Trammell G T and Hannon J P 1993 *Phys. Rev. Lett.* **71** 287
[13] Hill J P and McMorrow D F 1996 *Acta Crystallogr.* A **52** 236
[14] Gibbs D, Grübel G, Harshman D R, Isaacs E D, McWhan D B, Mills D and Vettier C 1991 *Phys. Rev.* B **43** 5663
[15] Lovesey S W, Fitz O and Balcar E 1998 *J. Phys.: Condens. Matter* **10** 501
[16] Schütz G, Knülle M, Wienke R, Wilhelm W, Wagner W, Kienle P and Frahm R 1988 *Z. Phys.* B **73** 67